# Observations of the Crab Nebula with the Chandra X-ray Observatory

**Martin C. Weisskopf**[*†]
*NASA/Marshall Space Flight Center, Huntsville, AL - USA*
*E-mail:* martin.c.weisskopf@nasa.gov

The Crab Nebula and its pulsar has been the subject of a number of detailed observations with the *Chandra* X-ray Observatory. The superb angular resolution of *Chandra*'s high-resolution telescope has made possible numerous remarkable results. Here we describe a number of specific studies of the Crab that I and my colleagues have undertaken. We discuss the geometry of the system, which indicates that the "inner X-ray ring", typically identified with the termination shock of the pulsar's particle wind, is most likely not in the equatorial plane of the pulsar. Other topics are the northern wisps and their evolution with time; the characterization of features in the jet to the southeast; pulse-phase spectroscopy and possible correlations with the features at other wavelengths, particularly the optical polarization; and a search for correlations of the X-ray flux with the recently-discovered $\gamma$-ray flares.

*An INTEGRAL view of the high-energy sky (the first 10 years) - 9th INTEGRAL Workshop and celebration of the 10th anniversary of the launch*
*15-19 October 2012*
*Bibliotheque Nationale de France, Paris, France*

[*]Speaker.

[†]I wish to recognize and thank my colleagues. Ring geometry: R.F. Elsner, J. J. Kolodziejczak, S.L. O'Dell, A.F. Tennant. Northern Wisps: T. Schweizer, N. Bucciantini, W. Idec, K. Nillson, A.F. Tennant, R. Zanin. Southern Jet: G. Pavlov, A.F. Tennant, K. Mori, S.L. O'Dell, D.A. Swartz, R.F. Elsner. Pulse-Phased Spectroscopy: A.F. Tennant, D.G. Yakovlev, A. Harding, V.E. Zavlin, S.L. O'Dell, R.F. Elsner, W. Becker. Search for the site of the $\gamma$-ray flares: A.F. Tennant, J. Arons, R. Blandford, R. Buehler, P. Caraveo, C.C. Cheung, E. Costa, A. de Luca, C. Ferrigno, H. Fu, S. Funk, M. Habermehl, D. Horns, J.D. Linford, A. Lobanov, C. Max, R. Mignani, S.L. O'Dell, R.W. Romani, E. Striani, M. Tavani, G.B. Taylor, Y. Uchiyama, & Y. Yuan.

## 1. Introduction

The Crab Nebula and its pulsar needs no lengthy introduction. The reader is referred to the excellent review by Hester [1] for historical details. We emphasize two more recent discoveries: Namely, the variability of the Nebula hard-X-ray energies on a few-year timescale [2] and the discovery of $\gamma$-ray flares using *AGILE* and *Fermi* [3, 4]

## 2. The Geometry: The pulsar is not at the center of the ring.

For this study, we analyzed *Chandra* zeroth-order images that used the Low-Energy Transmission Grating Spectrometer (left side of Figure 1). We draw your attention to the fact that the pulsar does not appear at the center of the ellipse. Although there are numerous possible explanations, we feel that displacing the "inner ring" surrounding the pulsar along the spin axis (right side of Figure 1) provides a reasonable interpretation. In this model, a circular ring of radius R is centered on the axis of symmetry of the pulsar wind nebula (PWN) - presumably the pulsar's spin axis. The line of sight to the observer is at a polar angle $\theta$ to the axis of symmetry, which is projected at a position angle $\psi$ (East of North) on the sky. By convention, we take the PWN's positive axis of symmetry z to lie in the northwest quadrant, so that $\psi \approx 300^{o}$. To resolve the ambiguity in the polar angle $\theta$, we interpret the brighter regions of the Crab torus to result from relativistic enhancement of emission from outflowing material [5]. Thus, the brighter regions of the torus are nearer the observer, which requires that $\theta \geq 90^{o}$ - i.e., we observe the "bottom" of the ring. Up to this point, the model is essentially the same as that used previously to de-project the X-ray inner ring (e.g., [6, 7, 8]), the X-ray torus [9], and visible-light structure [10, 1]. Note too that different magnetohydrodynamic calculations and simulations (e.g., [11, 12, 13, 14] and references therein)

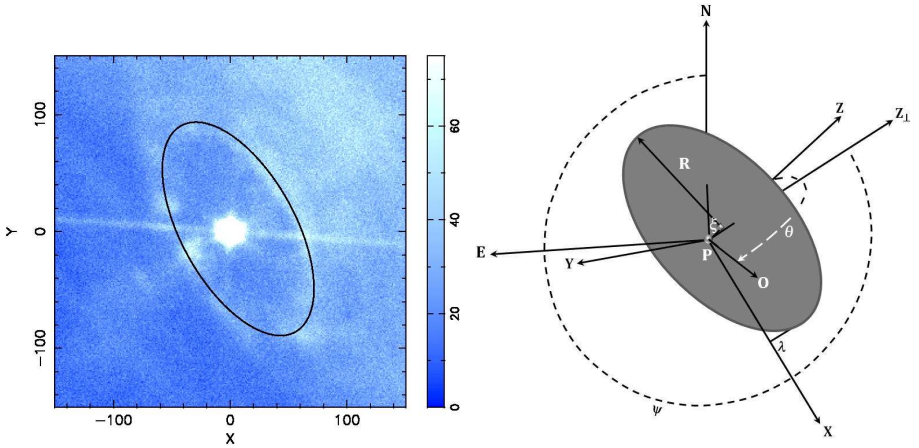


**Figure 1:** Left: *Chandra Low Energy Transmission Grating (LETG)/ High Resolution Camera - Spectroscopy detector (HRC-S)* zeroth-order image of the Crab Nebula (ObsIDs 758 and 759), over a $40'' \times 40''$ field centered on the pulsar. North is along the +Y axis; East, along the âĂŞX axis. The units are HRC pixels ($0.132''$). The approximately E-W streak results from diffraction (in the cross-dispersion direction) by support bars in the LETG facets. Right: Illustration of the geometrical model discussed in the text.

yield a torus-jet structure resulting from an equatorial striped wind. Here, however, the ring does not lie exactly in the equatorial plane of the pulsar, but rather at low (but non-zero) latitude $\lambda \approx 5^{o}$. We used two methods for determining the position of the ring. One was based on the peak flux, the other on the position of the inner edge. The results were similar if not identical. Using the inner edge we found: the radius of the inner-ring, $R = 13.25'' \pm 0.26''$; the polar angle from the symmetry axis to the line of sight, $\theta = 119.1^{o} \pm 1.0^{o}$; the position angle of the projected axis of symmetry (E of N), $\phi = 298.4^{o} \pm 1.1^{o}$; the axial distance along the symmetry axis from the pulsar to the plane of the inner ring, $\zeta = 1.04'' \pm 0.13''$; and the latitude of the inner ring, $\lambda = +4.49^{o} \pm 0.77^{o}$ (See [15] for further details.)

## 3. Northern Wisps

The 22 observations used for this study were taken with the back-illuminated CCD, ACIS-S3, over the time interval from MJD 55467.2 to 56181.9 (2010 Sep 28 - 2012 Sep 11). A frame time of 0.2 s was used to minimize pileup. Even so, pileup impacts the brighter regions of the nebula as may be seen in the image in the left side of Figure 2 where the pulsar appears as a "black hole" in the image being so piled up that the data are completely eliminated. Telemetry saturation also reduced the effective integration time. We restricted data to a $300 \times 300$ ACIS-pixel region ($\approx 150'' \times 150''$) centered on the pulsar. For the first 3 observations, the dither amplitude was set to zero; for the remainder it was set at $1''$.

Figure 2 left shows the *Chandra* ACIS S3 summed X-ray image of the inner portion of the Nebula (ObsIDs 13750-13754) with regions marked for study of the structure to the northwest of the pulsar. We refer to features to the northwest as "wisps". As in the optical, these structures

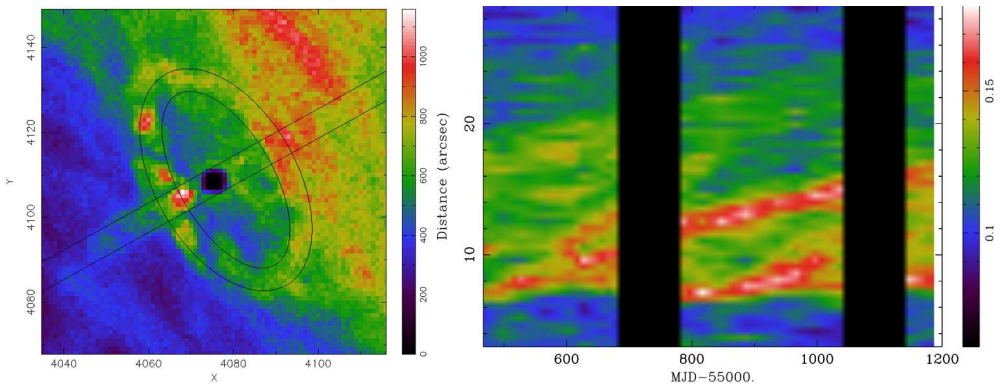


**Figure 2:** Left: Summed ACIS image of ObsIDs 131150-154. The $5''$-wide northwest portion of the rectangular box defines the region selected for studies of the radial distribution. The north-west portions of the $5''$-wide annular region determined by the inner and outer ellipses defines the region for studying the azimuthal distribution. Right: The time evolution of the radial structure to the northwest of the pulsar. The time spacing is 10 days. If an observation took place at any time within the 10-day interval, the data were included as a column in the figure. If there were short gaps in the time sequence, they were linearly averaged. Thus, if there was a two-column gap, for the first missing column we would add two thirds of the previous observation to one third of the next observation, etc.

appear to be constantly forming and breaking off from the innermost wisp, which is coincident with what we have referred to as the "inner ring" (e.g.[6]). The right side of Figure 2 shows the time evolution of the radial portions of the X-ray-emitting flux. There are at least 4 distinct progressions of the peak flux in the figure with deprojected radial velocities range from 0.14 to 0.5 v/c. The azimuthal profile of the innermost X-ray wisp has a broad width of tens of degrees which agrees well with predictions from magnetohydrodynamic modeling.

We are now in the process of comparing the X-ray view of the wisps with contemporaneous optical observations. The comparison is revealing and will, along with further details of the X-ray observations, be described in [16].

## 4. The Southern Jet

In this section we present a brief summary of spatial variations of the jet emanating to the southeast of the pulsar. Figure 3 shows two LETGS zero-order images taken 8 years apart. It is clear from the figure that the the jet has grown in length and changed shape in this time interval. We are in the process of completing an exhaustive study of all *Chandra* observations of the Crab spanning a 12-year time interval. We characterize the jet by determining, as a function of the distance from the pulsar, the Gaussian center, the Gaussian width, the peak surface brightness, and the length of the jet. Preliminary results are (the work will be described in detail in [17]) as follows:

- The direction of the jet undergoes a major change in position angle from about $120^{\circ}$ to about $140^{\circ}$ as the jet emerges from the synchrotron nebula.
- There is a second major shift in position angle that takes place at roughly $40'' - 50''$ from the pulsar. At this distance the jet reaches a maximum in position angle and then reverses direction.
- These latter reverses in position angle do not always take place at precisely the same distance from the pulsar and it is not clear whether the reversals follow some systematic variation with

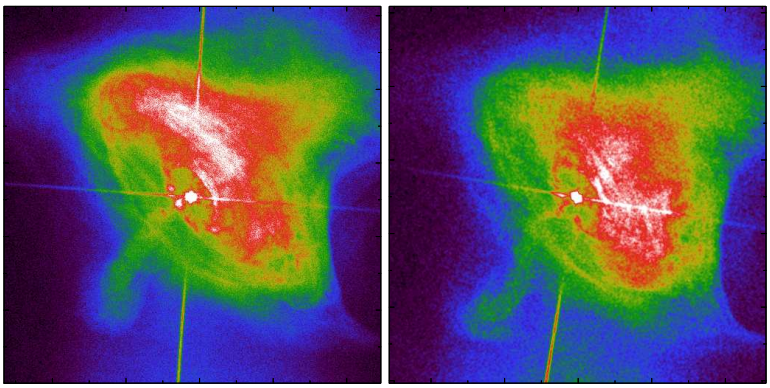

**Figure 3:** Left: The zero-order image from ObsID 759, taken in 2000 January. North is up and east is to the left. Right: The zero order image from ObsID 9765 taken in 2008 February. The almost vertical streak in both images is the dispersed grating spectrum of the pulsar. The orthogonal streak is the cross-dispersed grating spectrum of the pulsar.

time. If we assume a linear variation, the characteristic projected velocities are low, at about $v/c = 0.024$.

- The jet is kinky with numerous changes of apparent slope as a function of distance along the jet. Furthermore, a strong case can be made that once formed, a kink travels outward along the jet with characteristic projected velocities of $v/c \approx 0.1$.
- The width varies along the jet and the local maxima and minima do not always occur at the same location amongst different sets of observations. If one attributes this to motion, the projected velocity is $v/c \approx 0.001$ for the maxima and $v/c \approx 0.003$ for the minima.
- The distribution of the surface brightness along the jet is different at different times. If we ascribe these changes to linear motion, then the projected velocities are of the order of $v/c = 0.009$.
- The surface brightness predominately exhibits a single peak along the jet and all measurements appear to show hints of oscillatory variations with a characteristic separation between $7''$ and $17''$, depending on the observation.
- The jet is getting longer with time expanding at a projected velocity of $v/c \approx 0.03$.

## 5. Pulse Phase Spectroscopy

The superb angular resolution of *Chandra* enables distinguishing the pulsar from the surround-

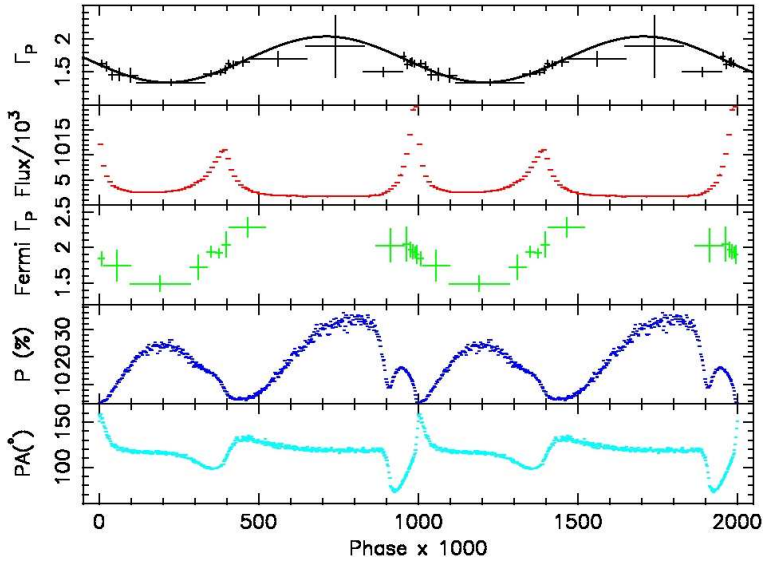


**Figure 4:** The top panel shows the measured variation of the X-ray powerlaw index with pulse phase. The solid curve in the upper panel results from fitting a sine wave plus a constant. The second panel from the top shows the X-ray light curve for reference (background not subtracted). The middle panel shows the variation of the $\gamma$-ray spectral index from [19]. The bottom two panels show the variation of the optical degree of polarization and position angle with phase from [20].

ing nebulosity and hence allows a fairly unbiased study of the pulsar. In [18] we utilized *Chandra*'s low-energy transmission grating spectrometer to perform spectroscopic observations of the pulsar, effectively isolated from the Nebula. We used the data for a number of purposes, including directly measuring the impact of scattering of flux out of the image by interstellar grains. We found the powerlaw index of the pulsed component to vary approximately sinusoidally, as shown in the upper panel of Figure 4. A potentially very exciting result of this study was that the only significant departure from the sinusoid occurs over the same phase range (near phase 0.9) as some rather abrupt behavior in the optical polarization magnitude and position angle and the hint of a similar feature in $\gamma$-rays (Figure 4).

More details, including unbiased upper limits to the surface temperature of the neutron star for different models of the atmosphere and a discussion relating such data to theoretical models of neutron star cooling and neutron star interiors, may also be found in [18].

## 6. Search for the Origin of the $\gamma$-ray Flares

Subsequent to announcements by the *AGILE* and by the *Fermi*-LAT teams of the discovery of $\gamma$-ray flares from the Crab Nebula in the fall of 2010, an international collaboration that we are leading has been monitoring X-ray emission from the Crab with *Chandra* on a regular basis. Observations typically occur once per month. In 2011 April, we also triggered a set of *Chandra* Target-of-Opportunity observations in conjunction with the brightest $\gamma$-ray flare yet observed. The aim of the program is to characterize X-ray variations within the Nebula, and, if possible, to precisely locate the origin of the $\gamma$-ray flares. Here we briefly summarize the results of the 2011 April X-ray observations.

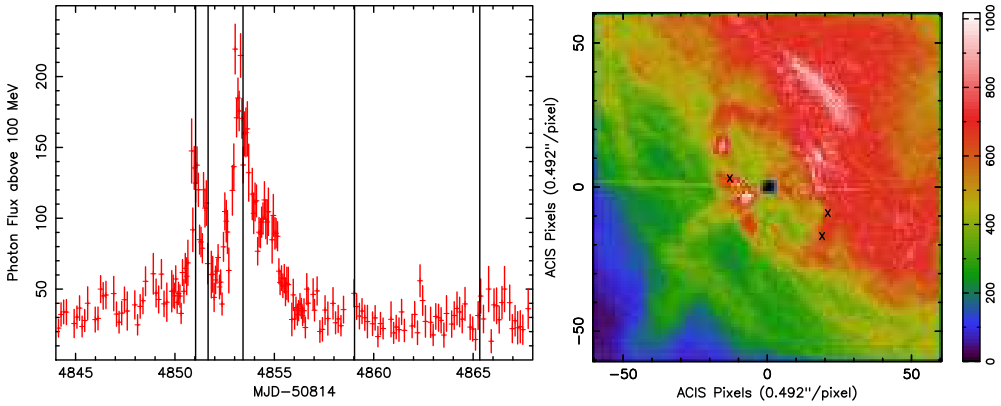


**Figure 5:** Left: *Fermi*-LAT photon flux ($10^{-7}$ ph/(cm$^2$ s)) above 100 MeV during the 2011-April flare as a function of time [21]. The vertical lines mark times of the 5 *Chandra* observations. Right: Summed count image for the 5 *Chandra* observations during the $\gamma$-ray flare. North is up, east to the left, and the pulsar is at (0,0). The nearly horizontal streak through the location of the pulsar is the trailed (out-of-time) image, resulting from the very short exposure of each pixel as the image is read out. As the 5 observations occurred at slightly different roll angles, the read-out streak is slightly blurred. The X symbols mark locations of the 3 statistically most significant variations, with the most significant being the one to the east of the pulsar.

**Table 1:** 99%-confidence upper limits for the analysis pixel with the most significant variation.

| $\Gamma_x$ | $\frac{2}{3}$ | 1 | 2 |
|---|---|---|---|
| $N_E[10^{-4}$ ph/(cm$^2$ s keV)] | 0.55 | 0.70 | 1.36 |
| $F_E[10^{-13}$ erg/(cm$^2$ s keV)] | 0.88 | 1.12 | 2.18 |
| $EL_E[10^{32}$ erg/s] | 0.42 | 0.54 | 1.05 |
| $\Gamma_{x\gamma}$ | 1.20 | 1.22 | 1.27 |

The five observations (ObsIDs 13150 – 13154) use the (back-illuminated) ACIS S3 CCD approximately centered on the Crab pulsar during and somewhat after the 2011-April $\gamma$-ray flare (Figure 5). Although standard processing typically produces an aspect solution better than $0.5''$, this small uncertainty still introduces noticeable shifts amongst different data sets; thus we re-registered images using the read-out streak and the hole produced by the piled up pulsar as guides.

The right side of Figure 5 shows the counts per ACIS pixel, summed over the 5 observations and binned a into a $60 \times 60$ array of $2 \times 2$ ACIS pixels centered on the pulsar . Each of these "analysis pixels" is sufficiently large to enclose most of the *Chandra* point spread function anywhere in the field of view.

We calculated the mean count rate $r_i$ averaged over the $J = 5$ observations, weighted[1] by the respective (counting-rate) statistical error $\sigma_{ij}$. Next we compute[2] $\chi^2_i$. Figure 5 indicates the location of the three pixels with the highest $\chi^2_i$. The most significant variation has $\chi^2_i = 23.5$ on $\nu = (J-1) = 4$ degrees of freedom. Such a fluctuation is expected in at least 1 of 3600 pixels in 31% of realizations and thus is *not* considered terribly significant. Based upon the $\chi^2$ probability distribution and the number of "tries", a 99%-confidence detection would require $\chi^2_{i,99\%} > 31.2$ on 4 degrees of freedom. While we detect no statistically significant variations at 99%-confidence, we note that the 3 most significant variations occur at bright locations on the inner ring.

Other effects, such as changes in the roll angle of the read-out streak, can lead to possibly spurious variability. This may be the case for the analysis pixel with the most significant variation, which lies adjacent to the average read-out streak (Figure 5).

Neglecting pile-up, the photon spectral flux is proportional to the count rate for an assumed spectral shape. Consequently, any change in count rate corresponds to a proportionate change in this flux. Using the *Chandra* PIMMS[3] for ACIS-S and an absorption column $N_{\rm H} = 3.1 \times 10^{21}$ cm$^{-2}$, we determine this constant of proportionality for a X-ray power-law photon index $\Gamma_x = \frac{2}{3}$, 1, and 2. Table 1 shows our calculations of the upper limits at 1-keV to the photon spectral flux $N_E(E_x)$, the energy spectral flux $F_E(E_x)$, and the indicative (isotropic) luminosity $EL_E(E_x) = 4\pi D^2 EF_E(E_x)$ at $D = 2$ kpc, for the analysis pixel with the most significant X-ray variation. Correcting for pile-up has little effect in low-count-rate regions, but would raise these flux upper limits by 10% or so for the high-count-rate regions.

We can also use the $\gamma$-ray data to quantify the implications of our lack of detection of time variations in the X-ray data. The approach compares a variability measure for the X-ray (1-keV)

[1] $r_i = \sum_{j=1}^{J}\{r_{ij}/\sigma_{ij}^2\}/\sum_{j=1}^{J}\{1/\sigma_{ij}^2\}$

[2] $\chi_i^2 = \sum_{j=1}^{J}\{(r_{ij}-r_i)^2/\sigma_{ij}^2\}$.

[3] http://asc.harvard.edu/toolkit/pimms.jsp

photon spectral flux $\Delta N_E(E_x)$ in each analysis pixel with the analogous variability measure for the $\gamma$-ray (100-MeV) photon spectral flux $\Delta N_E(E_\gamma)$. Based upon the sample standard deviation of the photon spectral flux at $E_x = 1$ keV for each X-ray analysis pixel and the measured standard deviation at $E_\gamma = 100$ MeV, we constrain the effective X-ray to $\gamma$-ray photon index of the flaring component: $\Gamma_{x\gamma} \equiv -\log[\Delta N_E(E_\gamma)/\Delta N_E(E_x)]/\log[E_\gamma/E_x]$. We compute 99%-confidence upper limits to $\Gamma_{x\gamma}$ (Table 1 last row). These limits are marginally consistent with the low-energy extrapolation of the $\gamma$-ray spectrum ($\Gamma_\gamma = 1.27 \pm 0.12$) of the flaring component [21]. More details may be found in a paper the team recently submitted to the Astrophysical Journal [22].

Finally, we note that the peak of the $\gamma$-ray flaring occurred at MJD 55000+667.425 (2011 April 16 10:12 UTC) and thus is *not* coincident with the peeling off of a northern wisp (Figure 2).

## References

[1] Hester, J.J. 2008, Annual Rev. Astron. & Astrophys., 46, 127.

[2] Wilson-Hodge, C.A., et al. 2011, ApJ, 727, L40

[3] Tavani, M., et al. 2011, Science, 331, 736

[4] Abdo, A.A., et al. 2011, Science, 331, 739

[5] Pelling, R.M., et al. 1987, ApJ, 319, 416

[6] Weisskopf, M.C., et al. 2000, ApJ, 536, L81

[7] Ng, C.Y. & Romani, R. W. 2004, ApJ, 601, 479

[8] Ng, C.Y. & Romani, R. W. 2008, ApJ, 673, 411

[9] Aschenback, B. & Brinkmann, W. 1975, A&A, 41, 147

[10] Hester, J.J. et al. 2002, ApJ, 577, L49

[11] Kennel, C.F., & Coroniti, F.V. 1984, ApJ, 283, 694

[12] Bogovalov, S.V. & Khangoulian, D. V. 2002, MNRAS, 336, L53

[13] Del Zanna, L., Amato, E., & Bucciantini, N. 2004, A&A, 421, 1063

[14] Kirk, J.G., Lyubarsky, Y., & Petri, J. 2009, Astrophysics and Space Science Library, 357, 421

[15] Weisskopf, M.C., et al. 2012, ApJ, 746, article id. 41

[16] Schweitzer, T., et al. 2013, to be submitted to MNRAS

[17] Weisskopf, M.C., et al. 2013, to be submitted to ApJ

[18] Weisskopf, M.C., et al. 2011, ApJ, 743, Issue 2, article id. 139

[19] Abdo, A. A., et al. 2010, ApJ, 708, 1254

[20] Slowikowska et al. 2008, in *HIGH TIME RESOLUTION ASTROPHYSICS: The Universe at Sub-Second Timescales*, AIP Conference Proceedings, 984, 51

[21] Buehler, R., et al. 2012, ApJ, 749, eid 26

[22] Weisskopf, M.C., et al. 2012, submitted to ApJ